Polarons in Metal Halide Perovskites

Daniele Meggiolaro,* Francesco Ambrosio, Edoardo Mosconi, Arup Mahata, and Filippo De Angelis*

Abstract

The peculiar optoelectronic properties of metal-halide perovskites, partly underlying their success in solar cells and light emitting devices, are likely related to the complex interplay of electronic and structural features mediated by formation of polarons. In this paper the current status of polaron physics in metal-halide perovskites is reviewed based on a first-principles computational perspective, which has delivered hitherto noaccessible insights into the electronic and structural features associated with polaron formation in this materials class. The role of organic (dipolar) versus inorganic (spherical) A-site cations is extensively analyzed, these cations are related to modulation of the energetics and structural extension of polarons in lead-halide perovskites. Further tuning of polaron energetics is achieved by individual variations in metal (e.g., Pb → Sn) and halide (e.g., I → Br), showing a transition from a semilocalized to a localized polaron regime in which charge holes can be trapped at isolated Sn centers. The vastly varying and tunable nature of charge lattice interactions represents a peculiarity of metal-halide perovskites that should be taken into account when designing novel materials or targeting specific compositional engineering of existing perovskites.

1 Introduction

Metal-halide perovskites, in particular lead-halide perovskites (LHPs), are promising materials for photovoltaics (PV) showing optimal optoelectronic properties, such as direct bandgaps and large absorption cross-sections.**1**-**3** The high efficiencies of these materials in solar cell devices are intimately related to the long lifetimes and diffusion length of charge carriers,**4**-**8** coupled to very low recombination rates even in the presence of fairly high defect densities typical of polycrystalline thin films.

The properties of photogenerated charge carriers in LHPs have been investigated by several authors.**9** Low carrier effective masses have been reported (≈0.1–0.2 m_e) in lead-iodide perovskites, related to low exciton binding energies.**5**, **10** Although a wide-spread of measured exciton binding energies is reported in the literature, in the range 2–62 meV for methylammonium lead iodide ($MAPbI_3$),**11** there is a general consensus in considering negligible the excitonic behavior at room temperature in this class of systems. The low exciton binding energies are comparable to those of highly efficient inorganic III–V semiconductors, such as GaAs, and are remarkably lower than the exciton binding energies measured in other emerging PV materials, such as conjugated polymers used in organic phtovoltaics and sensitizers used in dye-sensitized solar cells, which show exciton binding energies of hundreds of meV.**12**, **13** The low effective masses and the high static and dynamic lattice screening lead to the formation of Wannier–Mott excitons, thus the dynamics of carriers is close to a free-charge behavior.**5**, **9**, **14**-**17**

Rather low mobilities in the range 1–10^2 cm^2 V^{-1} s^{-1} have also been reported for LHPs.**4**, **18**-**20** The diffusion is dominated by electron-phonon scattering processes with low energy longitudinal-optical phonons associated to fluctuations of Pb□I bonds**21** and an inverse temperature dependence of the charge mobility $\mu \approx T^{-3/2}$ was reported.**17**, **22**, **23** Nevertheless, LHPs show very long carrier diffusion lengths (≈μm) and lifetimes (≈μs), coupled to low electron–hole recombination rates (10^{-10} cm^3 s^{-1}), comparable to those of pure single crystals inorganic semiconductors.

The origin of the low electron–hole recombination rate in solution-processed LHPs is still under debate. Monomolecular recombination promoted by lattice defects and grain boundaries only marginally affects

the efficiency of thin films used in solar cell devices, highlighting the high defect tolerance of this class of materials.**24**-**26** Several computational works clarified that large parts of native defects in LHPs are not active recombination centers due to their associated shallow character.**27**, **28** Charge trapping phenomena in LHPs are mainly related to under-coordinated halides,**29**-**33** but recent studies showed that trapping and recombination processes on these centers may be hindered by the existence of kinetic or thermodynamic barriers.**30**, **34**

The low bimolecular recombination rate and the modest mobility of charge carriers have not a clear origin and several hypotheses have been advanced. Among others, Rashba–Dresselhaus effects**35**, **36** have been proposed as a possible mechanism preventing the recombination due to the decreased recombination probability induced by the splitting in reciprocal space of valence and conduction band (CB) edges, turning the bandgap from direct to partly indirect.**35**, **37**, **38** These effects, however, require breaking the crystal inversion symmetry, which may be possibly accessible on fairly small nanodomains, of the order of few nm.**27**

The presence of organic cations in LHPs has suggested that the unconventional optoelectronic properties of these materials may be related to the disorder and rotational degrees of freedom associated to such organic cations. It has been proposed that poling of organic cations with the associated dipolar field can lead to formation of ferroelectric domains resulting in internal junctions promoting the charge separation and segregation and preventing radiative recombination.**39**-**43**

The formation of large polarons, as a result of the coupling between photogenerated charges and optical lattice phonons, has also been proposed as one of the most fascinating mechanism to explain the peculiar LHPs optoelectronic properties.**44**-**50** In the polaron model, electrons and holes are stabilized by different lattice deformations possibly localized in different spatial regions and the dynamic lattice screening prevents their recombination. Upon polaron formation the lattice deformation induced by the charge leads to the activation of particular phonon modes. In the original model proposed by Zhu and co-workers the reorientations of organic cations played a fundamental role in the dynamic screening of charges, responsible of the long time decay (>100 ps) of hot carriers associated to the slow thermalization process.**44**, **51**-**53** In this regard, it has been proposed that at higher excitation densities the slower cooling of hot phonons caused by large polarons overlapping can reheat the electronic degrees of freedom ("phonon-bottleneck") by overcoming the estimated theoretical efficiency of the material.**51**, **54**-**56**

In light of the huge interest stimulated by these initial works, it seems of interest to analyse in a unified framework some of the fundamentals and potential implications of polaronic models in LHPs. In this paper we thus review the basic principles and relevant models, along with experimental phenomenology, underlying the nature of polarons in LHPs. We do so from a first-principles computational perspective as these methods have allowed gaining unprecedented insight into the electronic and structural features of this class of materials.

2 Large Polarons—Static Vision: Lattice Rearrangement, Phonons, and Dimensions

Time-resolved optical Kerr effect spectroscopy estimated large polaron formation times in the range 0.3–0.7 ps in $MAPbBr_3$ and $CsPbBr_3$ perovskites, respectively.**50** Computational analyses based on density functional theory (DFT) provided additional insights into the basic polaron physics, in particular on its stabilization energy and the geometry of the lattice deformation, as well as the phonon modes activated in the process of polaron formation.

Charge holes were found to induce a remarkable rearrangement of the inorganic sub-lattice leading to a shortening of the Pb-halides bonds and to a reduction of the octahedral tilting. In **Figure 1**a the geometry and the energetics associated to this process in $CsPbBr_3$ are reported, as calculated by hybrid functional DFT.**50** By performing a projection of the lattice distortion induced by a charge hole onto the phonons eigen-modes calculated at Γ, it has been shown that phonon modes associated to stretching and bending of the inorganic cage are mainly activated by interaction with the charge (cf. Figure **1**b,c).**50** The activation of low energy bending modes upon polaron formation has been further confirmed by THz conductivity and transient Raman spectroscopy experiments on $CsPbBr_3$ and $MAPbI_3$ perovskites, respectively.**57**, **58** Notably, inorganic cations, like Cs, show larger polaron stabilization energies compared to organic cations. By using a large cubic $CsPbBr_3$ model we showed that the stabilized hole induces a large lattice distortion spreading over many unit cells (3–5 nm range) and localizing the charge in the region with shorter metal-halide bonds.**50**

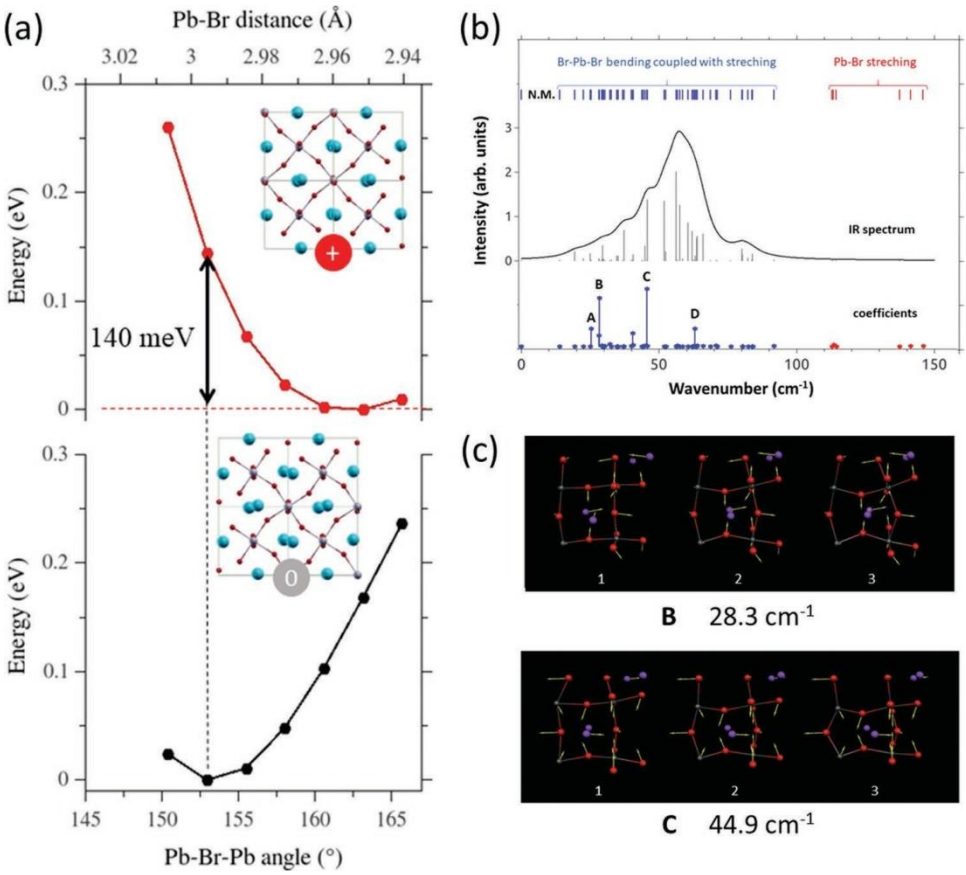

Figure 1 a) Lattice distortion induced by injected hole in $CsPbBr_3$ and associated polaron stabilization energy. b) IR spectrum and projection coefficients of the phonon modes activated by the displacement illustrated in (a). c) Graphical representation of the normal modes of the phonons with the highest coefficients in (b). Adapted with permission.50 Copyright 2017, AAAS.

Large polarons have a different impact on the carriers dynamics than “small polarons,” commonly encountered in, e.g., oxides and organics, where the structural distortion has a local character. Small polarons, whose formation is usually facilitated by the presence of lattice defects, strongly reduce the mobility of charge carriers by also activating charge-trapping processes with detrimental effects on the overall solar cell efficiency.**45**, **59** On the other hand, the partial delocalized nature of the charges is mostly associated to a bending of the band edges. In this context, the band-like behavior of the carriers dynamics

is essentially retained but with a heavier effective mass,**60**, **61** which, however, could still partially affect carrier mobility.**62**

Several computational works investigated the atomistic details of polarons in LHPs, both in 3D**58**, **63**, **64** as well as in 2D**65** and 0D perovskites. By using a DFT cluster approach Neukirch et al. demonstrated that localization of electrons and hole polarons is promoted by the orientation of organic cations and manifest through a stretching, compression of the octahedra Pb⍰I bonds, respectively.**63**, **64** However, high stabilization energies were reported by these authors.**63**, **64** Similar lattice distortions associated to the formation of electron and hole polarons have been found in 2D**65** and 0D perovskites.**66** Recently, using tight-binding methods on an extended perovskite model Zheng et al. reported that large polaron leads to a decrease of electron mobility by roughly a factor of two.**62**

In **Figure 2**, we illustrate the results achieved here for the size-dependent electronic properties of the hole polaron in $MAPbI_3$. We consider a structural configuration from a molecular dynamics (MD) simulation carried out on a 2 × 2 × 2 supercell of tetragonal $MAPbI_3$. Starting from this structure, we construct supercells of increasing lengths along the *z* direction (corresponding to the *c* crystal axis). Then, we relax the geometry employing full hybrid-DFT structural relaxations (see Section **8**). We observe that the polaron structures are retained in all the cases, as can be inferred from Figure **2**a,b, where the profiles of Pb⍰I distances and charge difference (neutral − positive) have been reported. The polaron localizes in the central plane, here arbitrarily set to 0, where the Pb⍰I distances are shorter than those of the neutral system. Pb⍰I distances gradually reach the value typical of the neutral system on planes far away from that in which most of the charge is localized.

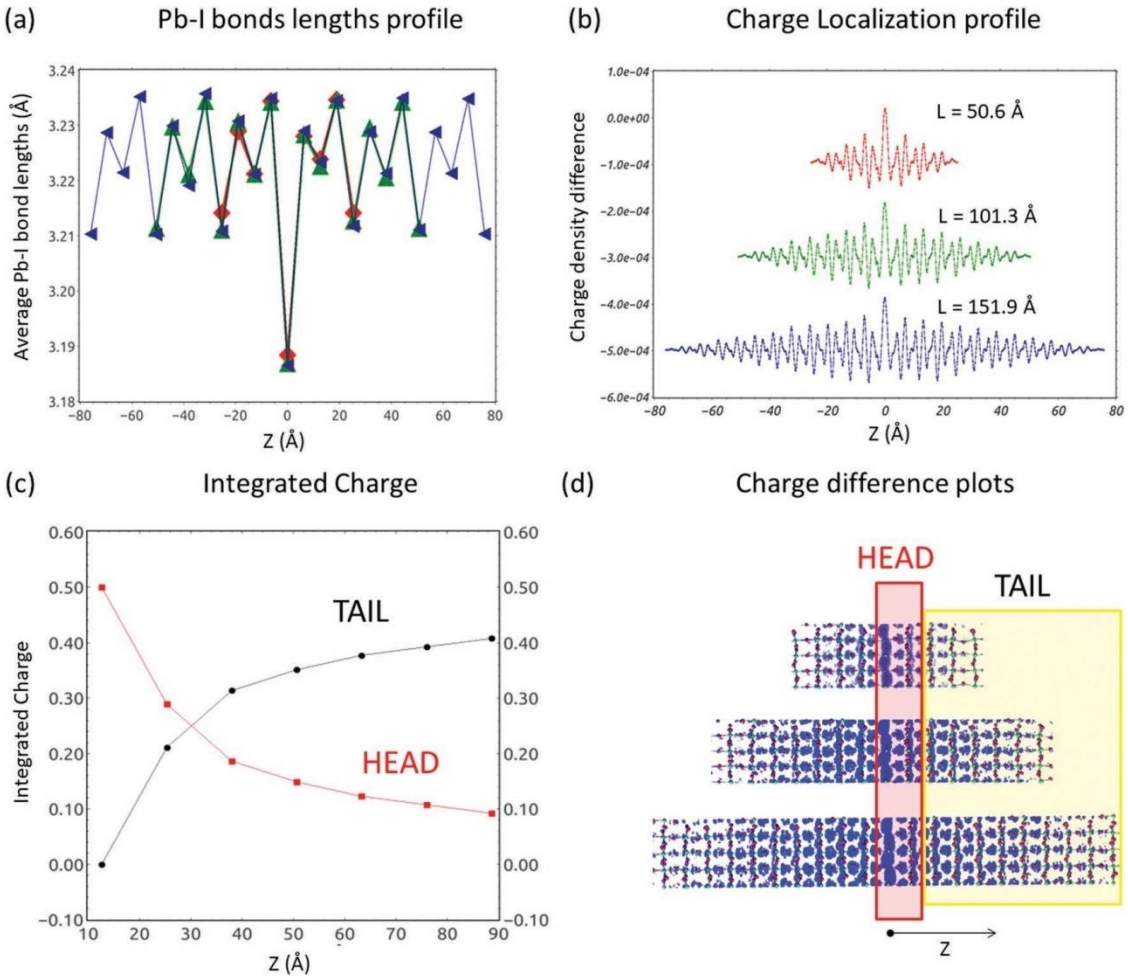

Figure 2 Hole polaron in $MAPbI_3$ simulated in supercells of increasing size; a) Pb–I average bond lengths profile. b) Planar average profile of the charge density difference along *z*. c) Integrated charge in the head and tail of polaron (cf. main text). d) Plots of the charge difference.

By increasing the size of the cell, a spread of the charge and associated distortion from the polaron plane into the supercell is reported, as shown in Figure **2**b. We calculate the integrated charge in two different volume portions of the simulated cells for models of increasing sizes along the *z* direction (cf. **Figure 3**c). The red points represent the integrated charge in a fixed volume enclosed between the polaron plane and a plane distant 12.6 Å from the former, i.e., the volume of a 2 × 2 × 1 supercell of bulk $MAPbI_3$ adjacent to the polaron plane [HEAD in Figure **2**d]. Black points represent the integrated charge in the remaining volumes of the supercells [TAIL in Figure **2**d]. As shown by the diagram, the integrated charge inside the volume in proximity of the polaron plane decreases by increasing the supercells sizes and reaches a value of ≈0.1 in the largest 2 × 2 × 14 simulated cell. On the other hand, the integrated charge in the remaining part of the supercell, i.e., the charge accumulated in the tail region of the polaron, increases by increasing the supercell size and reaches a value of 0.4. The maximum variations between the last three points of the diagram are ≈6% of the total charge. By this analysis, an equilibrium polaron radius of ≈60 Å can be estimated for $MAPbI_3$, about a factor two larger than that found in $CsPbBr_3$ in the limit of diluted charge carriers. Variations in the A-site cations and in the halide can clearly influence the polaron energetics and localization, as discussed later in this review. Charge analysis also highlights that in such conditions ≈20% of the charge is accumulated in the volume encompassing to the polaron plane (14% of charge is expected in the same volume for a delocalized carrier), while the remaining 80% is spread over the entire cell.

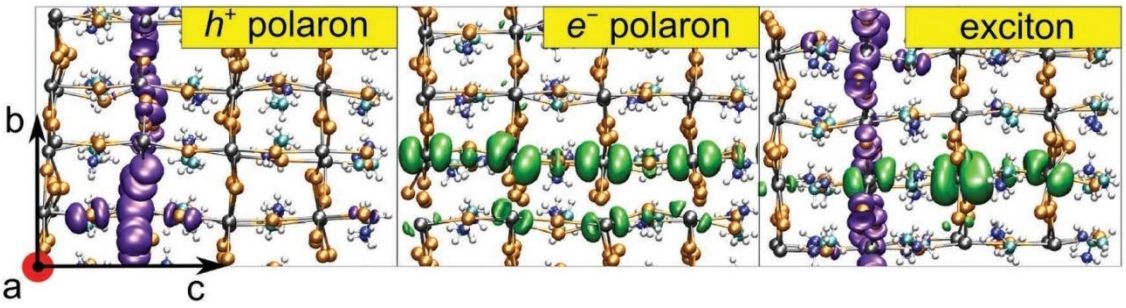

Figure 3 Isodensity representations of a hole polaron (left panel), an electron polaron (middle panel) and of an excitonic state (right panel) for tetragonal $CH_3NH_3PbI_3$. The tetragonal axis lies horizontally. Adapted with permission.96 Copyright 2018, RSC.

3 Large Polarons–Dynamic Vision: Molecular Dynamics Simulations

LHPs feature a sizable dynamic disorder at room temperature, which is due to both distortions in the soft inorganic sub-lattice and to the rotation and displacement of the A-site cations.**29**, **67**, **68** For this reason, modeling lead halide perovskite through molecular dynamics simulations is essential to properly investigate their coupled electronic and structural fluctuations.**69** The application of MD has been limited, however, to few cases, due to the significant computational burden associated to ab initio MD simulations.**70** In this context, theoretical studies have focused mainly on establishing the role of the organic cations in the modulation of the electronic properties of hybrid perovskites. For example, MD simulations enabled Mosconi et al. to reproduce the IR spectrum of $MAPbI_3$ methylammonium (MA) and to correlate the large fluctuations in the electronic bandgap (up to 0.2 eV) to the fluctuations of the inorganic sub-lattice induced by the MA cations.**71** More recent simulations have confirmed these results but have also underlined that the use of small periodic supercells brings to an overcorrelated motion of MA molecules, which would alter

their rotational dynamics.**72**-**74** Frost et al. postulated the occurrence of ferroelectric domains in $CH_3NH_3PbI_3$ induced by the polar cations, on the basis of MD and Monte Carlo simulations.**75** However, Quarti et al. performed MD simulations starting from polar (ferroelectric) and apolar (antiferroelectric) structures, showing that the latter are favored at room temperature.**76** This is motivated by the large disorder induced by the motion of the MA cations for apolar structures, a feature that is absent when the simulation is initiated from a polar configuration. MD simulations have been also deployed to understand the diffusion of defects in lead halide perovskites, in order to explain the peculiar defect tolerance observed for these materials. In this context, the use of ab initio simulations was found to produce only partial results, because of the limited time-scale (tens to hundreds of picoseconds at most) that can be actually sampled.**77**, **78** The recent development of force fields constructed specifically for hybrid perovskites**79**-**81** has allowed for longer simulations, otherwise unaffordable, which in turn enabled to calculate diffusion coefficients of point defects and also the thermal conductivity of $MAPbI_3$.**80**-**83**

In this framework, the study of polarons in LHPs through MD simulations has been introduced only recently in the literature, with the main scope of determining the physics underlying charge localization in this class of materials. Furthermore, the polaronic nature of charge carriers adds another layer of complexity to the perennial debate regarding the distinct roles of the inorganic sub-lattice and the A-site cations and their complex interplay, which determine the exceptional electronic properties of metal halide perovskites. An early attempt to connect the random orientation of the A-site cations to the localization of hole and electrons in $MAPbI_3$ was produced by Ma and Wang.**84** By combining Monte Carlo simulations with the linear scaling 3D fragment method,**85** they investigated the electronic structure of supercells up to >20.000 atoms.**84** Analysis of the band edges revealed a different nanoscale localization of the valence band (VBM) and conduction band (CBM), that the authors associated with fluctuations in the potential, caused by the erratic orientation of MA cations, and suggested to be responsible of the slow bimolecular recombination measured for $MAPbI_3$.**84** This interpretation was broadly shared by subsequent studies, which suggested polaron formation in $MAPbI_3$ to be promoted by the screening field of the organic cations.**46**, **86** Later measurements and simulations, while being at odds with the established physical picture, did not provide an undisputed explanation. On one side, time-resolved Kerr-effect experiments**50** and transient terahertz spectroscopy measurements**87** indicated that organic and fully inorganic perovskites share similar dynamics of polaron formation and charge recombination, thus suggesting that the role of the organic cations might have been overestimated or at least misinterpreted. First-principles MD simulations performed by Uratani and Yamashita on a set of different organic and fully inorganic lead iodide perovskites seemed to support the claim that organic cations do not significantly contribute to the physics of this class of materials.**88** By applying a methodology similar to that of ref. **84**, the authors stated that charge separation is induced by the structural fluctuations of the soft inorganic sub-lattice, provided, however, that charge carriers occupy the respective band edges.**88** On the other hand, solid-state magic angle spinning (MAS)-NMR measurements revealed that reorientation rates of MA and formamidinium (FA) in $(MA)_x(FA)_{1-x}PbI_3$ clearly correlate with the carrier lifetimes measured for materials bearing different MA/FA ratios.**89**, **90** In particular, FA favors longer carrier lifetimes, an occurrence explained by the authors in terms an easier formation of polarons made possible by a faster rotation of this cation.**89**, **90** Furthermore, Zheng and Wang refined the model proposed in ref. **84** in order to include polaronic effects and calculated a binding energy of 12 (55) meV for the electron polaron in absence (presence) of cationic disorder, thus again supporting the thesis of a central role of the organic cation.**62** In the same study, it was also proposed that the low mobility measured for charge carriers in $MAPbI_3$[21] derived from the balance between the random orientation of organic cations and the vibrations of the inorganic sub-lattice.**62**

Overall, the main drawback of most MD studies is the use of computational protocols featuring an approximated treatment of the electronic structure. In particular, the use of classical methods or of semilocal density functionals within ab initio techniques may severely limit the validity of the results achieved for charged systems, such as those necessary to simulate polarons in metal halide perovskites. In particular, the extension of charge localization and its energetics can be erroneously described by semilocal functionals, due to the self-interaction error.**91**, **92** This, however, can affect also calculations at the hybrid functional level, if the fraction of Fock exchange to be introduced in the functional is not correctly determined. Recently, the choice of hybrid functionals complying with the Koopman condition**93** has been successful in the determination of bandgaps and defect levels for semiconductors and insulators.**94**, **95**

Ambrosio et al. have employed this methodology and performed hybrid DFT-based molecular dynamics simulations, in order to provide a dynamical description of polaron formation and separation in $MAPbI_3$.**96** Simulations with an extra hole and an extra electron showed polaron formation on a sub-picosecond time scale, in excellent agreement with experimental data.**50**, **96** Furthermore, analysis of the wave function revealed a distinct spatial localization of hole and electron polaron. The former preferentially localizes on a Pb□I plane upon contraction of Pb□I bonds (Figure **3**), in accord with the antibonding hybridization of Pb 6s and I 5p orbitals,**97** which form the VBM. The latter is found to localize in 1D chains of Pb□I bonds (Figure **3**) which have undergone a significant elongation, a result coherent with the weak antibonding hybridization between Pb 6p and I 5p in the conduction band.**97** The calculated binding energies of 90 and 60 meV for electron and hole polaron, respectively, were found to be in accord with available measurements.**97** The study also investigated the physics of interacting charge carriers, by carrying out an MD simulation of $MAPbI_3$ in the presence of both an added electron and hole. It was shown that even in presence of Coulomb interaction between the charge carriers, these form polarons that are essentially localized in distinct regions of the material (Figure **3**). Analysis of the MD simulations illustrated clear connection between the orientation of the organic cations and the localization of the charge carriers. In contrast, the contribution of organic cations to the mechanism of charge separation was estimated to be only ancillary, with respect to the thermal motion of the inorganic sub-lattice, this interpretation being supported by the similar bimolecular recombination rates measured for hybrid and fully inorganic perovskites.**87** We note that in a more recent study, the nature of charge localization has been better clarified and it has been proved that this is induced by the disordered dipolar field of the A-site cations but stabilized mainly by distortions in the inorganic sub-lattice.**98**

The findings reported by Ambrosio et al. also allowed to rationalize some contrasting results in the literature. In fact, the agreement with the experiment observed for bimolecular recombination rates, when calculated assuming band-to-band transition,**99** does not apparently leave any room for the inclusion of polaronic effects.**46** However, the reduced overlap of charge carriers calculated by Ambrosio et al. was found to nicely compensate for the increased effective mass of polaronic charge carriers. In an ensuing work, Wiktor et al. have also explained the reduced recombination at defects in $MAPbI_3$ with the distinct localization of positive and negative charges.**34** They studied the process of charge trapping at the iodine interstitial through constrained MD simulations and verified the existence of a small barrier (70 meV) for hole–electron recombination at the defect site. This, in conjunction with the distinct spatial localization of the hole polaron and the negative charge localized on the interstitial, indicates a key role of polarons also in determining the surprising low mononuclear (trap-assisted) recombination rates**46**, **100** measured for $MAPbI_3$.

We note that the performed MD simulations sample time spans which are well below the sub-microsecond time scale measured for charge recombination. However, the time-dependent evolution of the polarons

with frequent hopping from plane to plane demonstrates that steady state conditions**96** are attained on the timescale of the simulations. This ensures that the structural configurations sampled by our simulations are representative of those occurring during the timescale pertaining to bimolecular recombination.**4**, **101** Therefore, MD configurations can be used to estimate the probability of the radiative transition, which is ultimately responsible for the long recombination timescale. This allows to connect the different timescales between polaron formation and bimolecular recombination.

4 Role of the A-Site Cations

Overall, remarkable advances have been achieved in reconciling the polaronic nature of charge carriers that have been recently demonstrated by both theory and experiments, with the previous and vast literature in which the peculiar optoelectronic properties of LHPs were showcased but only partially explained. In a recent contribution, Myung et al. have proposed that the coordination of organic cations to I atoms can be used to tune the properties of polarons in HPs.**102** However, the semilocal functionals employed to describe the electronic structure might not capture completely the physics of polarons in perovskites. Overall, the nature itself of polarons in this class of materials and the role of the organic cations is still lacking a comprehensive explanation. For example, one of the interesting features possibly previously overlooked**34**, **96** is the fast polaron hopping from one localization site to another. This peculiar phenomenon, found to occur on a sub-picosecond time-scale, is apparently in contrast with the low mobility of charge carriers measured for metal halide perovskites.**20** On this regard, some of us recently reported energy barriers of 150 and 80 meV for the hopping of hole and electron polarons, respectively, employing MD-generated structural configurations.**98** The hopping was found to occur through semilocalized electronic states [**Figure 4**a for the hole polaron]. These values allow for a prediction of the molecular motions involved in the charge-transfer process. However, a sub-nanosecond time-scale for polaron hopping was calculated from transition-state theory, when assuming the process to be promoted by the stretching of Pb–I bonds in $MAPbI_3$ (≈100 cm^{-1}),**21**, **103**-**105** a result in stark contrast with the sub-picosecond time-scale detected by the simulations. Furthermore, an inversion of the energy barriers is observed for an artificial system in which the MA cations have been removed. These results indicate that the inorganic sub-lattice cannot be considered the main agent promoting polaron hopping, on the contrary it would rather behave like an inorganic semiconductor**106** and favor a delocalized electronic state. Therefore, the role of A-site cations has to be reconsidered also to explain polaron hopping. In this framework, the correlative analysis of MD simulations carried out for $MAPbI_3$ and for an artificial system in which MA cations had been considerably weighted down permitted to unambiguously understand the physics underlying polaron hopping in lead halide perovskites. In fact, the mass of the hydrogen atoms of the MA cations is increased 12-fold in the artificial system (referred to as h-$MAPbI_3$, cf. Figure **4**c), and polaron formation is found to be drastically slower. Furthermore, the time-dependent evolution of charge localization denoted an absence of polaron hopping throughout the entire simulation (cf. Figure **4**b,c). A comparative structural analysis of the time-dependent rearrangement of MA cations indicated that the slower and reduced variation of the dipole field within the h-$MAPbI_3$ system lead to this phenomenon. This, in conjunction with MD simulations on $FAPbI_3$, allowed to provide a consistent explanation for the measured correlation**89**, **90** between diffusion lengths and rotation times of cations. Furthermore, it also provided a qualitative explanation for the low mobility of charge carriers measured for lead halide perovskites. In fact, since the motion of A-site cations is significantly influenced by neither the presence of extra charges nor an external electric field, fast and random hopping governs charge transfer within the material. We note that, when the MA cation is substituted with Cs, larger stabilization energies are calculated for the polarons (vide infra, cf. Section **6**). A more strongly bound polaron would suggest a lower mobility of the charge carriers. However, this is in contrast with studies showing that the substitution of

MA with an inorganic cation improves the mobility of carriers.**70**, **107**, **108** This can be indeed connected with the present results. In fact, the substitution of MA with Cs does not only contribute to the polaron stabilization but also changes the extent and the frequency of the fluctuations of the dipole field induced by A-site cations.**98** The fast and random hopping is likely to be more hindered in perovskites bearing the slower Cs cations. In turn, the system can be more sensitive to an external electric field, thus bringing to increased values of carriers' mobility.

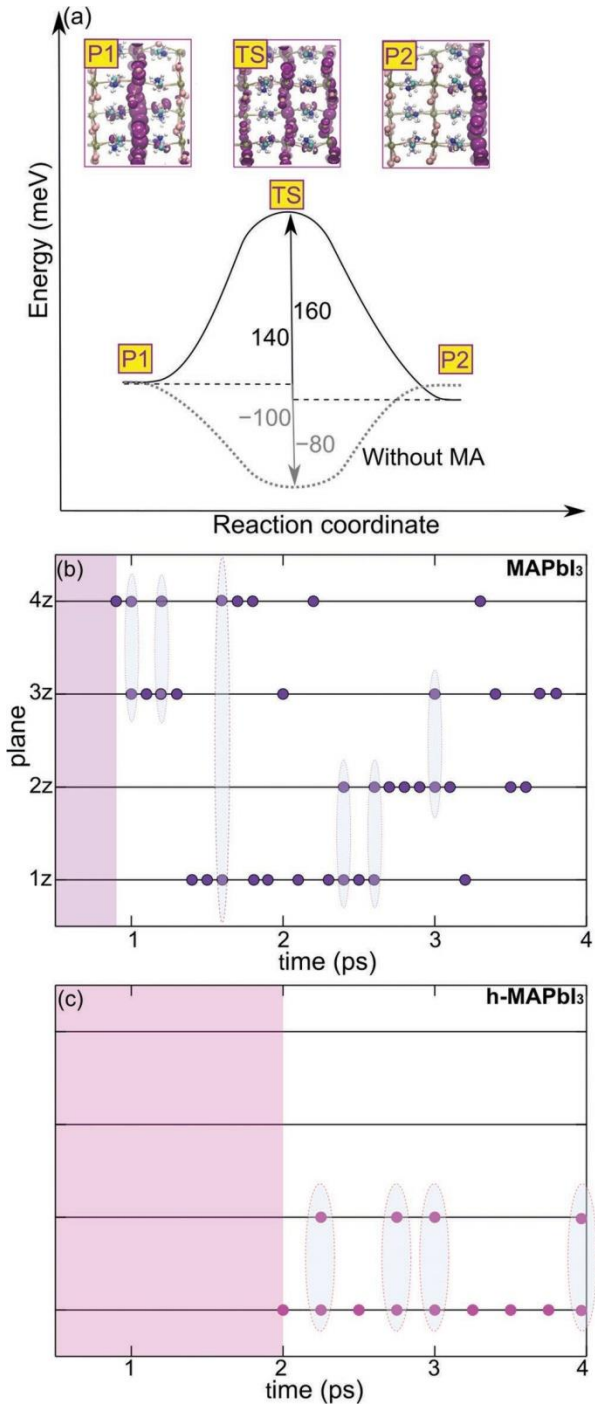

Figure 4 a) Reaction energy profile illustrating the hole diffusion through adjacent Pb□I planes. Isodensity representations of the wave functions are given for the polaronic structures (P1 and P2) and for the transition state (TS). Dotted gray lines represent the energy diagrams achieved from calculations in which the MA cations have been removed. Time-dependent charge localization of the hole polaron for a) regular $MAPbI_3$ and c) h-$MAPbI_3$ (cf. main text). The hole density localizes in planes of the inorganic sub-lattice

orthogonal to the tetragonal axis (labeled 1z to 4z). Therefore, each point of the diagram represents the instantaneous position of the hole polaron as inferred from analysis of the wave function. Cyan circles highlight configurations in which the hole is shared among adjacent planes. The shaded areas highlight the time span before hole localization. Adapted with permission.98 Copyright 2013, ACS.

5 Impact of Organic Cation Fluctuation on Charge Localization

The orientation of the organic cations is probably the most complex problem in the structural characterization of hybrid organohalide perovskites. In this section, we focus the attention on the interplay between the cation orientation and the charge localization in LHPs based on Car-Parrinello molecular dynamics (CPMD) simulations on $MAPbI_3$ and $FAPbI_3$.**71**, **76**, **109**

The cubic α phase and the tetragonal β-phase of $MAPbI_3$ are simulated by a 2 × 2 × 2 supercell using the experimental cell parameters. In particular, three tetragonal structures different in the starting orientation of the MA cations are adopted and reported in **Figure 5:109** MA β1 is characterized by an isotropic orientation of the MA cations within the *ab*-plane, and an anisotropic orientation with respect to the *c*-axis, with the MA cations tilted by ≈30° with respect to the *ab*-plane. The β2 and β3 model show an isotropic distribution of the MA cations both with respect to the *ab*-plane and along the *c*-axis and there are thus paraelectric.

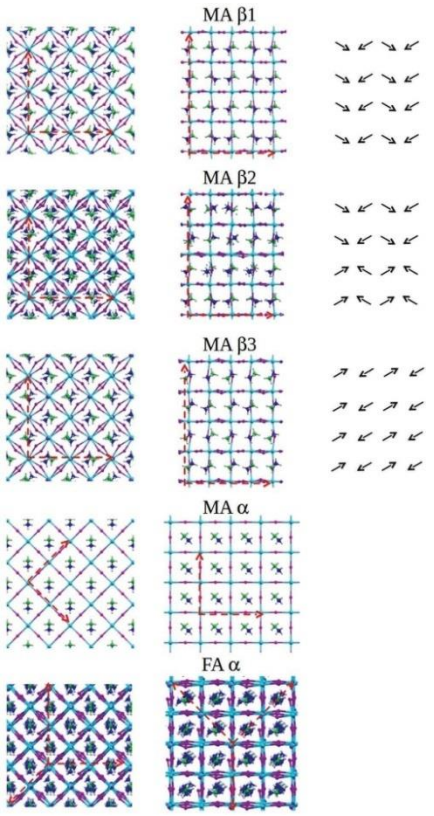

Figure 5 Top view and side view of the structural models for the $MAPbI_3$ and $FAPbI_3$: the tetragonal β-phase of $MAPbI_3$ (MA β1,2,3) and the cubic-α phase of $MAPbI_3$ (MA α) and the triclinic, pseudocubic-α phase of $FAPbI_3$ (FA α). For the tetragonal MA β1,2,3 structures, we report also the starting orientation of the MA cations as black arrows (right panels). The red arrows represent the cell parameters. Reproduced with permission.109 Copyright 2015, RSC.

For $FAPbI_3$, α-phase, here on FAα, is simulated with a 2 × 2 × 2 supercell of the XRD experimental trigonal structure from ref. **2**.

For all the structures, together with the bandgap, we calculated also the density of states (DOS) and the contributions from all the atoms within the reference cell, i.e. the projected density of states (pDOS), on selected snapshot along the CPMD trajectories. Then, for the β-phase of $MAPbI_3$ we estimated the delocalization of the frontier electronic states along the [001] direction, i.e., along the nonsymmetric cell parameter, by summing the contributions from the inorganic atoms lying on the same crystallographic plane. In this way, we obtained the local DOS associated with a specific *i*th layer, DOS*i*(*t,E*).

In **Figure 6**, we report the DOS$_i$(*t,E*) for MA β3, in the energy range of the frontier levels, calculated for two consecutive geometries extracted from the first-principles MD simulations (time difference 0.06 ps)**109** and the arrows indicate the spatial localization of the valence band (VB) and CB edge. As shown in Figure **6**, in the first geometry, the VB and CB edges are clearly localized in the layers lying respectively at 12.66 and at 0.00 Å. After just 0.06 ps instead, the localization of the electronic states is different, with the valence and conduction band edges localized respectively on the 6.33 and 18.99 Å lying layers. Thus, Figure **6** points out that the valence and conduction band edges may localize in spatially separated regions with a very fast, sub-ps, dynamics.**109**

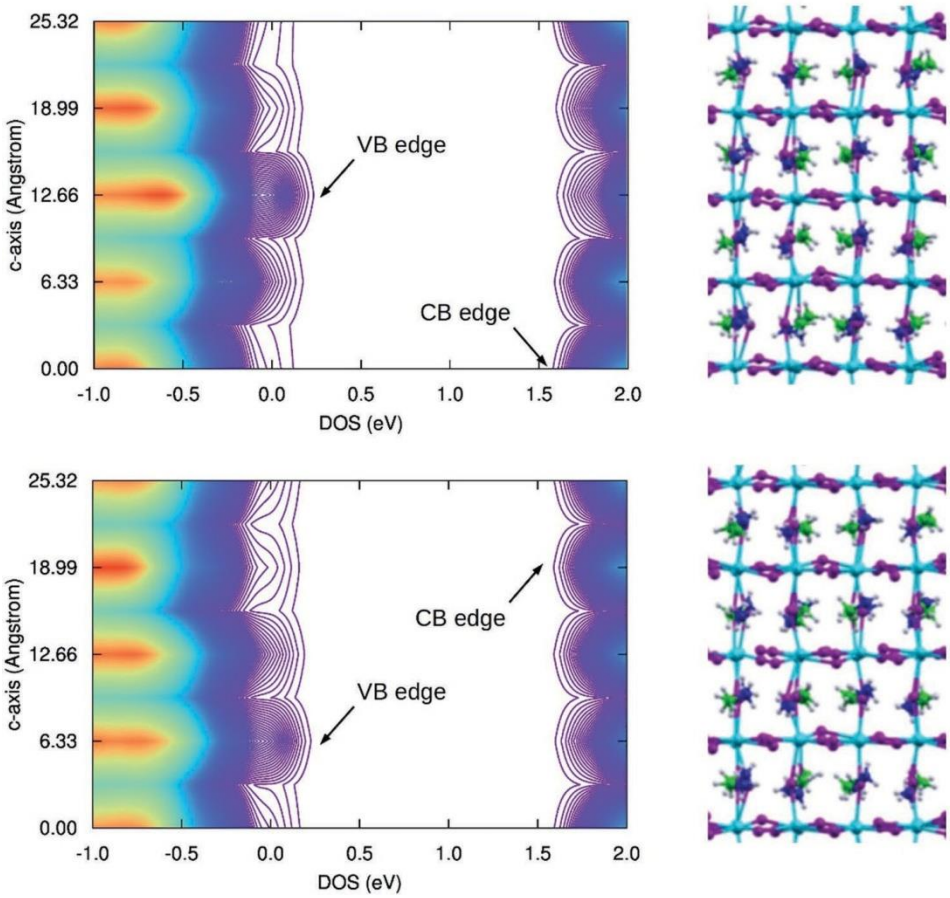

Figure 6 Surface plot of the density of states of the valence and conduction states for the various layers within the reference cell, for the MA β3 structure, for two consecutive geometries (0.06 ps time difference). The corresponding structure is reported on the right. The arrows indicate the spatial localization of the valence band (VB) and conduction (CB) edge. Reproduced with permission.109 Copyright 2015, RSC.

This effect could play an important role on the photovoltaic working mechanism of $MAPbI_3$, for instance, in relation to the exciton and/or charge separation mechanism.**15**, **110** Figure **6** suggests in fact that, subsequently to the photon absorption, the photogenerated species may diffuse in spatially separated regions of the material. DFT calculations reported by Ma et al.**84** pointed out a similar space-localization of the valence and conduction states of the $MAPbI_3$ perovskite, as a result of the random orientation of the MA cations.

For each structure, we provide a general picture on the localization of the electronic states among the various layers, during the MD simulations. To quantify the electronic localization layer-by-layer, we calculate $q_i(t,E)$, that corresponds to the difference between the number of states at the lowest unoccupied molecular orbital (LUMO) energy, $DOS_i(t,E = \text{LUMO})$, and the number of states at the highest occupied molecular orbital (HOMO) energy, $DOS_i(t,E = \text{LUMO})$, for the *i*th layer; in mathematical form

$$q_i(t) = DOS_i(t, E = \text{LUMO}) - DOS_i(t, E = \text{HOMO}) \quad (1)$$

This q_i(t) function describes the VB and CB localization and the charge separation upon photoexcitation. In a hypothetical perfectly homogeneous system where the VB and CB are not localized, qi(t) is expected to be the constant in the material, while if q_i(t) shows positive (negative) values this corresponds to an excess of conduction (valence) states in a given layer. The evolution of the $q_i(t,E)$ parameter defined in Equation **1** for the investigated structures is reported in **Figure 7** and it shows that the spatial localization of the valence and conduction band edges in a specific layer, as that reported in Figure **6**, is quite common. Moreover, it confirms that the present mechanism is characterized by sub-ps dynamics (≈200 cm^{-1}), that is reasonably related to the libration motions of the MA cations. In ref. **110**, Even et al. suggested a role of collective MA cation motions on exciton screening, leading to almost free charges. Once again, the limited dimension of our models, mainly imposed by the computational cost of our approach, does not allow to catch the effect of collective MA motions. Anyway, our MD simulations highlight a very local effect of the motion of the organic cations on the electronic properties, resulting in the separation of the electronic states within a few pseudocubic units.

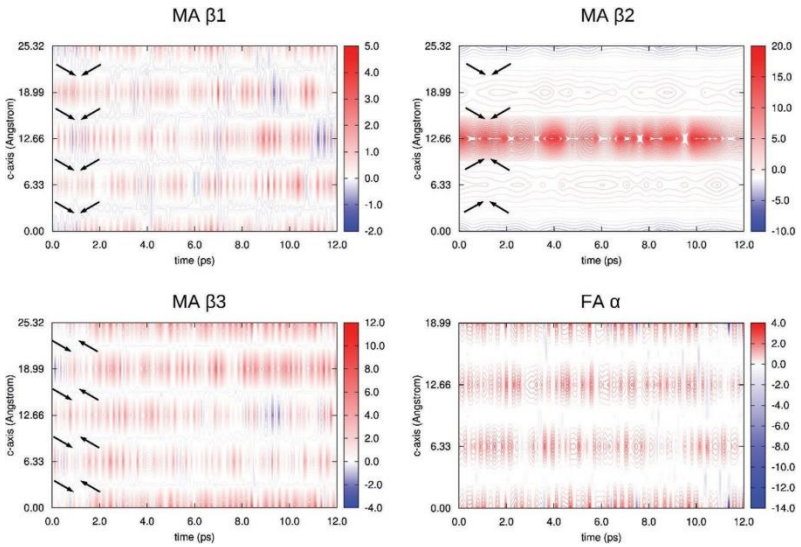

Figure 7 Evolution of the $q_i(t)$ parameter (i.e., the difference between the number of states calculated at the LUMO and HOMO energy) for the MA β1,2,3, and FAα structures. The arrows between 0 and 2 ps represent the starting orientation of the MA cations, for the MA β1,2,3 structures. Reproduced with permission.109 Copyright 2015, RSC.

In general, we observe a more effective localization for the conduction states against valence states. It is interesting to note that MA β1, characterized by the lower mobility of the MA cation, shows the smallest variations for $q_i(t,E)$, between 5 and −2. The MA β3 structure, characterized by more mobile MA cations, shows much larger oscillations for $q_i(t,E)$, between 12 and −4. The present result highlights once more the importance of the dynamic disorder on this dynamically driven state separation mechanism. The FAα phase, characterized by the largest orientational mobility of the organic cations, shows the smallest oscillation of the $q_i(t,E)$ parameter, between 3.5 and −1.5, excluding sporadic cases with a very strong localization of the valence states. It is worth to note that the smallest degree of charge separation, i.e., smallest values of $q_i(t,E)$, are found for the model with the smaller and the larger mobility of the MA cations, MA β1 and FAα. This result points out on different localization mechanisms for the tetragonal and the cubic phase of hybrid, lead iodide perovskites. The rationale behind this result could be the aforementioned weakening of the hydrogen bonds, going from the tetragonal to the cubic structure that results in a less effective, hydrogen-bond induced, localization of the electronic states.

We found that the dynamic disorder from the ionic motion have important consequences on the electronic properties of hybrid, lead halide perovskites. The analysis of the localization of the electronic states demonstrates that a spatial separation of the valence and conduction states takes place in hybrid perovskites, during the molecular dynamic simulations. Such charge localization is obviously associated to an easier charge separation process but can be also at the basis of the small charge recombination rates found in $MAPbI_3$.**6**

In other words, we address such spatial localization not to a static and disordered orientation of the organic cations but to their inherent rotational dynamics within the cubo-octahedral cavity. Thus, the mechanism of exciton screening due to the dynamics of the MA cation, hypothesized by Even et al. in ref. **110** finds here a demonstration from electronic structure calculations.

6 Effect of Chemical Modifications: Varying A, B, and X

The effects of chemical composition on the polaron physics in perovskites has been only partially explored, but this is a prominent issue due to the wide interest in tuning the chemical composition of this class of materials toward specific optoelectronic properties with potential applications in several fields, from solar cells to light emission. In this section, an overview of the individual and combined effects of A, B, and X substitution on the polaron stabilization energy is provided. A wide computational study of the effects of substitution on the polaron stabilization energies and the resulting coupling with the lattice phonons has been carried out by Mahata et al.**111**

The role of organic cations on the polaron dynamics has been discussed in the previous sections. Recently, the impact of cations on the charge carriers dynamics and recombination attracted a raised interest due to the practice of using cations alloys in order to increase the stability of perovskites.**112** By performing DFT calculations, Mahata et al. investigated the stabilization energies of holes injection in the prototypical $MAPbI_3$ perovskite and on other systems bearing different organic/inorganic cations (i.e., FA and Cs and mixed MA, Cs). Based on hybrid functional calculations, it has been found that FA leads to polarons stabilization energies comparable with those achieved with MA cations, while the use of inorganic (and smaller) cations (i.e. Cs) produces larger rearrangements of the lattice upon polaron formation with associated larger stabilization energies (see **Table 1**).**111** Also, the alloying of $MAPbI_3$ with Cs linearly increases the polaron stability by confirming the trend showed by single cation perovskites. The effects of cations on the polaron stabilities are mainly indirect and are mediated by the distortion of the inorganic sub-lattice. Cations with larger radiuses, such as MA and FA, physically hinder the shrinking of the inorganic

lattice upon hole injection. In the case of organic cations, hydrogen bonds further reduce the flexibility of the Pb□I inorganic network. This reflects in small stabilization energies of the polaron (≈50 meV) and more limited shortening of the Pb□I bonds. On the other hand, smaller and apolar cations like Cs allow for larger deformation of the inorganic and the gained flexibility in the Pb□I bonds results in higher stabilization energies, i.e., double than those estimated for perovskites bearing organic cations.**111**

Table 1. Polaron stabilization energy for different metal-halide perovskites. Some values are replicated in the rows for better understanding the trend111

Systems	Polaron stabilization energy [meV]	
	+1	−1
Variations in A-site cations		
$MAPbI_3$	46	6
$FAPbI_3$	47[a)]	5
$Cs_{0.25}MA_{0.75}PbI_3$	52	9
CsPbI	96	0
Variations in X-site anion		
$MAPbI_3$	46	6
$MAPbBr_3$	60	10
$CsPbBr_3$	161	10
Variations in B-site cation		
$MAPbI_3$	46	6
$MASnI_3$ [3]	75	35
$CsSnI_3$	188	57
Variations in mixed B-site cation		
$MAPbI_3$	46	6
$MAPb_{0.75}Sn_{0.25}I_3$	155	29
$MAPb_{0.50}Sn_{0.50}I_3$	97	65
$MAPb_{0.50}Sn_{0.50}I_3$ -diagonal	92	8
$MAPb_{0.25}Sn_{0.75}I_3$	80	68
$MASnI_3$	75	35

[a)]The value has been scaled by ¾ to account for the same charge density.

The impact of metal substitution has gained a huge interest due to the possibility of increasing the stability of the lattice,**74**, **80**-**82** reducing the toxicity and tuning the perovskite bandgap.**113**-**120** In particular, mixed Pb–Sn perovskites represent an interesting model system. In fact, while recent studies suggest that the inclusion of Sn might not substantially reduce the toxicity of the system,**121**-**123** long carriers lifetimes and fairly high efficiencies have been reported in mixed Pb–Sn perovskites.**124** These results represent a remarkable advance toward the development of all-perovskite tandem solar cells.**117**, **125**

The substitution of Pb by Sn in $MAPbI_3$ increases the polaron stabilization energies independently of the Sn content in the perovskite, by showing larger stabilization energies for decreasing values of the Sn doping (see Table **1**). In order to investigate the polaron behavior in Sn-lightly doped $MAPbI_3$, the hole polaron stabilization energies in the 25% and 3% Sn-doped systems have been recalculated in the 2 × 2 × 2 supercell at the PBE0 level of theory (see Section **8**). Stabilization energies of 82 and 20 meV are reported for the Sn-3% and Sn-25% doped perovskites, respectively. After rescaling for the modeled density of carriers in the cells (stabilization energies in Table **1** are calculated in the single unit cell) a stabilization energy for Sn-25% doped system of 158 meV is obtained, in good agreement with result in Table **1**. Interestingly, these results show that by increasing the Sn content the stabilization energy does not vary uniformly, but it shows a maximum for a Sn small percentage (Sn-3% doped $MAPbI_3$), comparable to densities commonly employed in doping procedures. The large polaron stabilization energies are coupled to remarkable distortion of the Sn–I octahedra in the mixed Pb–Sn–I inorganic sub-lattice. As an example, at small Sn percentages shortenings of two equatorial Sn□I bonds of the octahedra of 0.14 and 0.21 Å are found, while the maximum shortening of Pb□I bonds lengths of the same plane for $MAPbI_3$ is of 0.08 Å. The plot of the hole state in such system confirms the localization of the hole density on the octahedron surrounding the Sn atoms (see **Figure 8**). By increasing the Sn content in the perovskites, a progressive delocalization of the hole density in the cell and a decrease of the stabilization energy is observed, as highlighted by Figure **8**. This finding is in agreement with the analysis of the electronic structures of doped systems, showing the electronic states due to Sn closer in energy to the VBM with respect to the Pb states, due to the lower redox potential of Sn compared to Pb. The origin of the strong polaron localization in lightly doped Sn $MAPbI_3$ can be traced back to the asymmetries in the distribution on bond lengths across different layers, leading to preferential polaron “nucleation” in the layer where shorter metal-halide bonds are present, i.e., Sn□I bonds. By this analysis, we observe a transition from a regime in which the hole is semilocalized in $MAPbI_3$ to a strongly localized polaron in Sn-doped LHP at low concentration, with sizable impact on the

charge recombination and efficiencies. Finally, an increased concentration of Sn leads to a more delocalized hole in the system, similarly to that observed for the pristine $MAPbI_3$ case.

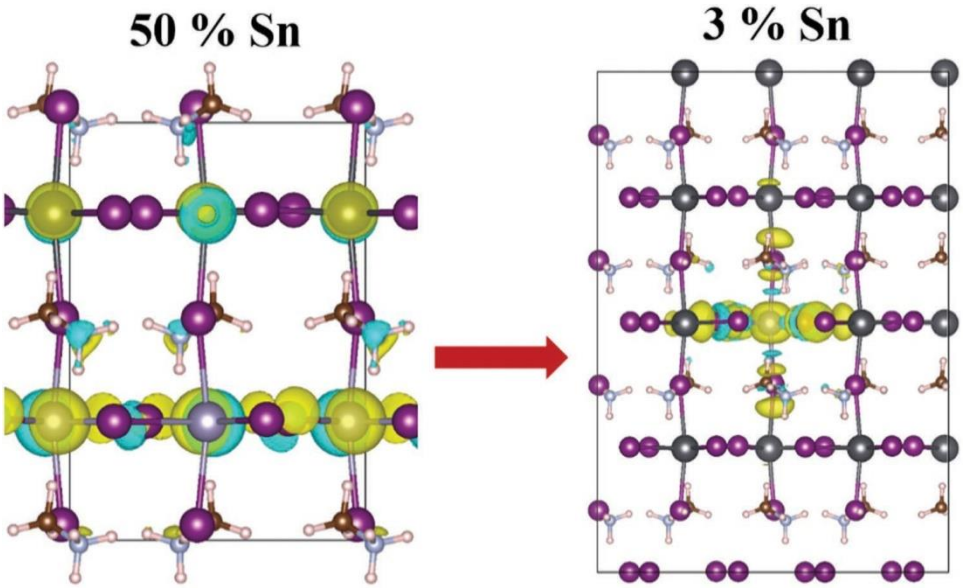

Figure 8 Plot of the charge density difference of holes polaron for 50% and 3% content of Sn in $MAPbI_3$, highlighting the different extent of charge localization. Adapted with permission.111 Copyright 2019, ACS.

The local nature of polaron in lightly Sn-doped system assumes the character of a self-trapped state that may increase the nonradiative monomolecular recombination leading to a decrease of the charge carriers' lifetimes in the crystal. Summarizing, metal dopants contents should be judiciously considered since even small percentage can have detrimental effects for the efficiencies of the device.

Variations in the X halide are also expected to lead to quantitative differences in the polaron physics, due to the changes in the bandgaps and the ionicity of the bonds. In this regard, while iodide perovskites are promising materials for applications in solar cell devices, bromide and chloride perovskites are interesting for lighting applications.**126**-**129** By focusing on halide substitution, generally larger polaron stabilization energies are reported in bromide, compared to iodide perovskites (see Table **1**).**111** This behavior can be associated to the higher ionicity and the reduced screening of charges in bromides, when compared to iodide perovskites. We note that the larger stabilization energy calculated for Br-containing perovskite is consistent with the trends observed from recently estimated values of carriers' mobility for $CsPbX_3$ (X = I, Br, Cl).**108**

7 Conclusions and Outlook

We have reviewed the current status of polaron physics in metal-halide perovskites based on a first-principles computational perspective. These techniques have proven extremely useful in providing hitherto inaccessible insight into the electronic and structural features associated to polaron formation in this materials class. Particular emphasis has been posed on the role of organic (dipolar) versus inorganic (spherical) A-site cations. While the electronic properties are only marginally affected by the different nature of the A-site cations, they are definitely found to modulate the energetics and structural extension of polarons in LHPs. Most notably, dynamic disorder promoted by fluctuations of A-site cations produces a complex potential energy surface which tends to separate electrons and holes, in the form of the respective polarons, inducing a significantly reduced charge carrier recombination at the expense of a reduced carrier mobility. Besides A-site cations, further tuning of polaron energetics is achieved by

individual variations in metal (e.g., Pb → Sn) and halide (e.g., I → Br). Of particular relevance for applicative purposes, mixed Pb/Sn perovskites can feature trap states at isolated Sn centers in which holes can be strongly localized. The vastly varying and tunable nature of charge lattice interactions represents a peculiarity of metal-halide perovskites that should be taken into account when designing novel materials or targeting specific compositional engineering of existing perovskites.

8 Computational Details

DFT calculations in Figure **2** have been carried out on the tetragonal phase of $MAPbI_3$ by using the freely available CP2K suite of codes.**130** In order to study hole-polarons of increasing size, 2 × 2 × *n* supercells have been built starting from an hole-polaron 2 × 2 × 2 supercell extracted by an hybrid functional (PBE0) MD simulation.**96** This structure was relaxed at 0 K in the positive and neutral charged states by using the PBE0 functional.**131**, **132** Then, supercells of increasing size 2 × 2 × *n* along the *z* direction were built by adding neutral-relaxed 2 × 2 × 2 supercell units to one single positive-relaxed supercell. Hole polarons have been simulated introducing single positive charges in the 2 × 2 × *n* supercells and by performing geometry optimizations with the hybrid PBE0 functional, by relaxing ions positions and fixing the lattice parameters to the experimental values $a = b = 8.86$ Å, $c = 12.66$ Å.**133** Hybrid functional PBE0 calculations have been performed by keeping the fraction of Fock exchange α at its original value (0.25) and by including nonlocal van der Waals interactions through the rVV10 scheme.**134**, **135** Calculations have been carried out with Goedecker–Teter–Hutter pseudopotentials to account for core–valence interactions.**136** We use double-ζ polarized basis sets for the wave functions**137** and a cutoff of 300 Ry for the expansion of the electron density in plane waves. We used the auxiliary density matrix method with the cFIT auxiliary basis set to speed up the hybrid functional calculations.**137**

Polaron stabilization energies of Sn-3% and Sn-25% doped systems discussed in Section **6** have been calculated in the 2 × 2 × 2 supercell of tetragonal $MAPbI_3$ by using the CP2K package and the PBE0 functional, by adopting the same computational setup described above, but without including van der Waals interactions. Sn-3% and Sn-25% doped systems were simulated by substituting 1/32 and 8/32 Pb ions by Sn in the pristine 2 × 2 × 2 supercells, respectively. Supercells with Sn-dopants were firstly relaxed in their neutral states. Then, hole polarons were modelled by introducing single positive charges in the neutral relaxed supercells by relaxing ions positions and keeping cell parameters fixed to the experimental values. Polarons stabilization energies are calculated as the relaxation energies of the positive supercells starting from the respective neutral relaxed structures, i.e. $-[E^+(+)-E^+(0)]$, where $E^+(+)$ is the energy of the positive relaxed supercell and $E^+(0)$ is the energy of the neutral relaxed supercell in the 1+ state of charge.

Acknowledgements

The authors acknowledge support from the Ministero Istruzione dell'Università e della Ricerca (MIUR) and the University of Perugia through the program “Dipartimenti di Eccellenza 2018–2022” (grant AMIS) and from the European Union's Horizon 2020 research and innovation programme under Grant Agreement No 764047 of the Espresso project.

Conflict of Interest

The authors declare no conflict of interest.

Biographies

Daniele Meggiolaro received his Ph.D. in Chemistry at "La Sapienza" University of Rome (Italy) in 2015. Currently, he is researcher at the Computational Laboratory for Hybrid/Organic Photovoltaics (CLHYO), CNR-SCITEC of Perugia (Italy). His research activity is focussed on the computational modelling of innovative materials for energy production and storage, with emphasis on photovoltaics materials and Li-ion batteries.

Francesco Ambrosio is a post-doctoral researcher at the Istituto Italiano di Tecnologia. He graduated in Chemistry at Universita' degli Studi di Napoli "Federico II". In 2014 he received his Ph.D. in Chemistry from the University of Warwick (UK). He worked as a post-doctoral researcher at École polytechnique fédérale de Lausanne until 2018. His present research activity is focussed on molecular dynamics simulations of polarons in lead halide perovskites.

Filippo De Angelis is Professor of Chemistry at the University of Perugia (Italy) and leader of the Computational Laboratory for Hybrid/Organic Photovoltaics (CLHYO - **www.clhyo.org**). Most of his recent research includes the computational modelling of solar energy materials, with emphasis on water splitting, dye-sensitized, and perovskite solar cells.

References

- 1 M. A. Green, A. Ho-Baillie, H. J. Snaith, *Nat. Photonics* 2014, **8**, 506.
- 2 C. C. Stoumpos, C. D. Malliakas, M. G. Kanatzidis, *Inorg. Chem.* 2013, **52**, 9019.
- 3 E. Mosconi, A. Amat, M. K. Nazeeruddin, M. Graetzel, F. De Angelis, *J. Phys. Chem. C* 2013, **117**, 13902.
- 4 S. D. Stranks, G. E. Eperon, G. Grancini, C. Menelaou, M. J. P. Alcocer, T. Leijtens, L. M. Herz, A. Petrozza, H. J. Snaith, *Science* 2013, **342**, 341.
- 5 A. Miyata, A. Mitioglu, P. Plochocka, O. Portugall, J. T.-W. Wang, S. D. Stranks, H. J. Snaith, R. J. Nicholas, *Nat. Phys.* 2015, **11**, 582.
- 6 C. Wehrenfennig, G. E. Eperon, M. B. Johnston, H. J. Snaith, L. M. Herz, *Adv. Mater.* 2014, **26**, 1584.
- 7 A. R. S. Kandada, A. Petrozza, *Acc. Chem. Res.* 2016, **49**, 536.
- 8 S. Poncé, M. Schlipf, F. Giustino, *ACS Energy Lett.* 2019, **4**, 456.
- 9 C. Wehrenfennig, M. Liu, H. J. Snaith, M. B. Johnston, L. M. Herz, *J. Phys. Chem. Lett.* 2014, **5**, 1300.
- 10 P. Umari, E. Mosconi, F. De Angelis, *J. Phys. Chem. Lett.* 2018, **9**, 620.
- 11 L. M. Herz, *Annu. Rev. Phys. Chem.* 2016, **67**, 65.
- 12 R. Kersting, U. Lemmer, M. Deussen, H. J. Bakker, R. F. Mahrt, H. Kurz, V. I. Arkhipov, H. Bässler, E. O. Göbel, *Phys. Rev. Lett.* 1994, **73**, 1440.
- 13 M. Knupfer, *Appl. Phys. A* 2003, **77**, 623.
- 14 Q. Lin, A. Armin, R. C. R. Nagiri, P. L. Burn, P. Meredith, *Nat. Photonics* 2015, **9**, 106.

- 15 V. D'Innocenzo, G. Grancini, M. J. P. Alcocer, A. R. S. Kandada, S. D. Stranks, M. M. Lee, G. Lanzani, H. J. Snaith, A. Petrozza, *Nat. Commun.* 2014, **5**, 3586.
- 16 S. Sun, T. Salim, N. Mathews, M. Duchamp, C. Boothroyd, G. Xing, T. C. Sum, Y. M. Lam, *Energy Environ. Sci.* 2014, **7**, 399.
- 17 T. J. Savenije, C. S. Ponseca, L. Kunneman, M. Abdellah, K. Zheng, Y. Tian, Q. Zhu, S. E. Canton, I. G. Scheblykin, T. Pullerits, A. Yartsev, V. Sundström, *J. Phys. Chem. Lett.* 2014, **5**, 2189.
- 18 G. Xing, N. Mathews, S. Sun, S. S. Lim, Y. M. Lam, M. Grätzel, S. Mhaisalkar, T. C. Sum, *Science* 2013, **342**, 344.
- 19 D. Shi, V. Adinolfi, R. Comin, M. Yuan, E. Alarousu, A. Buin, Y. Chen, S. Hoogland, A. Rothenberger, K. Katsiev, Y. Losovyj, X. Zhang, P. A. Dowben, O. F. Mohammed, E. H. Sargent, O. M. Bakr, *Science* 2015, **347**, 519.
- 20 T. M. Brenner, D. A. Egger, A. M. Rappe, L. Kronik, G. Hodes, D. Cahen, *J. Phys. Chem. Lett.* 2015, **6**, 4754.
- 21 A. D. Wright, C. Verdi, R. L. Milot, G. E. Eperon, M. A. Pérez-Osorio, H. J. Snaith, F. Giustino, M. B. Johnston, L. M. Herz, *Nat. Commun.* 2016, **7**, 11755.
- 22 H. T. Yi, X. Wu, X. Zhu, V. Podzorov, *Adv. Mater.* 2016, **28**, 6509.
- 23 M. Karakus, S. A. Jensen, F. D'Angelo, D. Turchinovich, M. Bonn, E. Cánovas, *J. Phys. Chem. Lett.* 2015, **6**, 4991.
- 24 A. Zakutayev, C. M. Caskey, A. N. Fioretti, D. S. Ginley, J. Vidal, V. Stevanovic, E. Tea, S. Lany, *J. Phys. Chem. Lett.* 2014, **5**, 1117.
- 25 W.-J. Yin, T. Shi, Y. Yan, *Adv. Mater.* 2014, **26**, 4653.
- 26 K. X. Steirer, P. Schulz, G. Teeter, V. Stevanovic, M. Yang, K. Zhu, J. J. Berry, *ACS Energy Lett.* 2016, **1**, 360.
- 27 W.-J. Yin, T. Shi, Y. Yan, *Appl. Phys. Lett.* 2014, **104**, 063903.
- 28 A. Buin, R. Comin, J. Xu, A. H. Ip, E. H. Sargent, *Chem. Mater.* 2015, **27**, 4405.
- 29 D. Meggiolaro, F. De Angelis, *ACS Energy Lett.* 2018, **3**, 2206.
- 30 D. Meggiolaro, S. G. Motti, E. Mosconi, A. J. Barker, J. Ball, C. Andrea Riccardo Perini, F. Deschler, A. Petrozza, F. De Angelis, *Energy Environ. Sci.* 2018, **11**, 702.
- 31 M.-H. Du, *J. Phys. Chem. Lett.* 2015, **6**, 1461.
- 32J.-S. Park, J. Calbo, Y.-K. Jung, L. D. Whalley, A. Walsh, *ACS Energy Lett.* 2019, **4**, 1321.
- 33 L. D. Whalley, R. Crespo-Otero, A. Walsh, *ACS Energy Lett.* 2017, **2**, 2713.
- 34 J. Wiktor, F. Ambrosio, A. Pasquarello, *J. Mater. Chem. A* 2018, **6**, 16863.
- 35 T. Etienne, E. Mosconi, F. De Angelis, *J. Phys. Chem. Lett.* 2016, **7**, 1638.

- 36 M. Kepenekian, R. Robles, C. Katan, D. Sapori, L. Pedesseau, J. Even, *ACS Nano* 2015, **9**, 11557.
- 37 K. Frohna, T. Deshpande, J. Harter, W. Peng, B. A. Barker, J. B. Neaton, S. G. Louie, O. M. Bakr, D. Hsieh, M. Bernardi, *Nat. Commun.* 2018, **9**, 1829.
- 38 X. Zhang, J.-X. Shen, W. Wang, C. G. Van de Walle, *ACS Energy Lett.* 2018, **3**, 2329.
- 39 J. M. Frost, K. T. Butler, F. Brivio, C. H. Hendon, M. v. Schilfgaarde, A. Walsh, *Nano Lett.* 2014, **14**, 2584.
- 40 S. Liu, F. Zheng, N. Z. Koocher, H. Takenaka, F. Wang, A. M. Rappe, *J. Phys. Chem. Lett.* 2015, **6**, 693.
- 41 J. Jankowska, O. V. Prezhdo, *J. Phys. Chem. Lett.* 2017, **8**, 812.
- 42 Y. Kutes, L. Ye, Y. Zhou, S. Pang, B. D. Huey, N. P. Padture, *J. Phys. Chem. Lett.* 2014, **5**, 3335.
- 43 H.-S. Kim, S. K. Kim, B. J. Kim, K.-S. Shin, M. K. Gupta, H. S. Jung, S.-W. Kim, N.-G. Park, *J. Phys. Chem. Lett.* 2015, **6**, 1729.
- 44 H. Zhu, K. Miyata, Y. Fu, J. Wang, P. P. Joshi, D. Niesner, K. W. Williams, S. Jin, X.-Y. Zhu, *Science* 2016, **353**, 1409.
- 45 X. Y. Zhu, V. Podzorov, *J. Phys. Chem. Lett.* 2015, **6**, 4758.
- 46 Y. Chen, H. T. Yi, X. Wu, R. Haroldson, Y. N. Gartstein, Y. I. Rodionov, K. S. Tikhonov, A. Zakhidov, X. Y. Zhu, V. Podzorov, *Nat. Commun.* 2016, **7**, 12253.
- 47 K. Miyata, T. L. Atallah, X.-Y. Zhu, *Sci. Adv.* 2017, **3**, e1701469.
- 48 M. Bonn, K. Miyata, E. Hendry, X. Y. Zhu, *ACS Energy Lett.* 2017, **2**, 2555.
- 49 T. Ivanovska, C. Dionigi, E. Mosconi, F. De Angelis, F. Liscio, V. Morandi, G. Ruani, *J. Phys. Chem. Lett.* 2017, **8**, 3081.
- 50 K. Miyata, D. Meggiolaro, M. T. Trinh, P. P. Joshi, E. Mosconi, S. C. Jones, F. De Angelis, X. Y. Zhu, *Sci. Adv.* 2017, **3**, e1701217.
- 51 M. B. Price, J. Butkus, T. C. Jellicoe, A. Sadhanala, A. Briane, J. E. Halpert, K. Broch, J. M. Hodgkiss, R. H. Friend, F. Deschler, *Nat. Commun.* 2015, **6**, 8420.
- 52 D. Niesner, H. Zhu, K. Miyata, P. P. Joshi, T. J. S. Evans, B. J. Kudisch, M. T. Trinh, M. Marks, X. Y. Zhu, *J. Am. Chem. Soc.* 2016, **138**, 15717.
- 53 Z. Guo, Y. Wan, M. Yang, J. Snaider, K. Zhu, L. Huang, *Science* 2017, **356**, 59.
- 54 K. Chen, A. J. Barker, F. L. C. Morgan, J. E. Halpert, J. M. Hodgkiss, *J. Phys. Chem. Lett.* 2015, **6**, 153.
- 55 Y. Yang, D. P. Ostrowski, R. M. France, K. Zhu, J. van de Lagemaat, J. M. Luther, M. C. Beard, *Nat. Photonics* 2016, **10**, 53.
- 56 J. M. Frost, L. D. Whalley, A. Walsh, *ACS Energy Lett.* 2017, **2**, 2647.

- 57 E. Cinquanta, D. Meggiolaro, S. G. Motti, M. Gandini, M. J. P. Alcocer, Q. A. Akkerman, C. Vozzi, L. Manna, F. De Angelis, A. Petrozza, S. Stagira, *Phys. Rev. Lett.* 2019, **122**, 166601.
- 58 M. Park, A. J. Neukirch, S. E. Reyes-Lillo, M. Lai, S. R. Ellis, D. Dietze, J. B. Neaton, P. Yang, S. Tretiak, R. A. Mathies, *Nat. Commun.* 2018, **9**, 2525.
- 59 H. Diab, G. Trippé-Allard, F. Lédée, K. Jemli, C. Vilar, G. Bouchez, V. L. R. Jacques, A. Tejeda, J. Even, J.-S. Lauret, E. Deleporte, D. Garrot, *J. Phys. Chem. Lett.* 2016, **7**, 5093.
- 60 H. Zhu, M. T. Trinh, J. Wang, Y. Fu, P. P. Joshi, K. Miyata, S. Jin, X. Y. Zhu, *Adv. Mater.* 2017, **29**, 1603072.
- 61 T. J. S. Evans, K. Miyata, P. P. Joshi, S. Maehrlein, F. Liu, X. Y. Zhu, *J. Phys. Chem. C* 2018, **122**, 13724.
- 62 F. Zheng, L.-w. Wang, *Energy Environ. Sci.* 2019, **12**, 1219.
- 63 A. J. Neukirch, I. I. Abate, L. Zhou, W. Nie, H. Tsai, L. Pedesseau, J. Even, J. J. Crochet, A. D. Mohite, C. Katan, S. Tretiak, *J. Phys. Chem. Lett.* 2018, **9**, 7130.
- 64 A. J. Neukirch, W. Nie, J.-C. Blancon, K. Appavoo, H. Tsai, M. Y. Sfeir, C. Katan, L. Pedesseau, J. Even, J. J. Crochet, G. Gupta, A. D. Mohite, S. Tretiak, *Nano Lett.* 2016, **16**, 3809.
- 65 D. Cortecchia, J. Yin, A. Bruno, S.-Z. A. Lo, G. G. Gurzadyan, S. Mhaisalkar, J.-L. Bredas, C. Soci, *J. Mater. Chem. C* 2017, **5**, 2771.
- 66 J. Yin, P. Maity, M. De Bastiani, I. Dursun, O. M. Bakr, J.-L. Brédas, O. F. Mohammed, *Sci. Adv.* 2017, **3**, e1701793.
- 67 D. A. Egger, A. M. Rappe, L. Kronik, *Acc. Chem. Res.* 2016, **49**, 573.
- 68 J. M. Frost, A. Walsh, *Acc. Chem. Res.* 2016, **49**, 528.
- 69 J. M. Frost, K. T. Butler, F. Brivio, C. H. Hendon, M. van Schilfgaarde, A. Walsh, *Nano Lett.* 2014, **14**, 2584.
- 70 A. Mattoni, A. Filippetti, C. Caddeo, *J. Phys.: Condens. Matter* 2016, **29**, 043001.
- 71 E. Mosconi, C. Quarti, T. Ivanovska, G. Ruani, F. De Angelis, *Phys. Chem. Chem. Phys.* 2014, **16**, 16137.
- 72 M. A. Carignano, A. Kachmar, J. Hutter, *J. Phys. Chem. C* 2015, **119**, 8991.
- 73 C. Goehry, G. A. Nemnes, A. Manolescu, *J. Phys. Chem. C* 2015, **119**, 19674.
- 74 J. Lahnsteiner, G. Kresse, A. Kumar, D. D. Sarma, C. Franchini, M. Bokdam, *Phys. Rev. B* 2016, **94**, 214114.
- 75 J. M. Frost, K. T. Butler, A. Walsh, *APL Mater.* 2014, **2**, 081506.
- 76 C. Quarti, E. Mosconi, F. De Angelis, *Chem. Mater.* 2014, **26**, 6557.

- 77 S. Meloni, T. Moehl, W. Tress, M. Franckevičius, M. Saliba, Y. H. Lee, P. Gao, M. K. Nazeeruddin, S. M. Zakeeruddin, U. Rothlisberger, M. Graetzel, *Nat. Commun.* 2016, **7**, 10334.
- 78 E. Mosconi, F. De Angelis, *ACS Energy Lett.* 2016, **1**, 182.
- 79 A. Mattoni, A. Filippetti, M. I. Saba, P. Delugas, *J. Phys. Chem. C* 2015, **119**, 17421.
- 80 X. Qian, X. Gu, R. Yang, *Appl. Phys. Lett.* 2016, **108**, 063902.
- 81 T. Hata, G. Giorgi, K. Yamashita, *Nano Lett.* 2016, **16**, 2749.
- 82 P. Delugas, C. Caddeo, A. Filippetti, A. Mattoni, *J. Phys. Chem. Lett.* 2016, **7**, 2356.
- 83 C. Caddeo, C. Melis, M. I. Saba, A. Filippetti, L. Colombo, A. Mattoni, *Phys. Chem. Chem. Phys.* 2016, **18**, 24318.
- 84 J. Ma, L.-W. Wang, *Nano Lett.* 2015, **15**, 248.
- 85 L.-W. Wang, Z. Zhao, J. Meza, *Phys. Rev. B* 2008, **77**, 165113.
- 86 A. Walsh, *J. Phys. Chem. C* 2015, **119**, 5755.
- 87 S. Dastidar, S. Li, S. Y. Smolin, J. B. Baxter, A. T. Fafarman, *ACS Energy Lett.* 2017, **2**, 2239.
- 88 H. Uratani, K. Yamashita, *J. Phys. Chem. C* 2017, **121**, 26648.
- 89 D. J. Kubicki, D. Prochowicz, A. Hofstetter, P. Péchy, S. M. Zakeeruddin, M. Grätzel, L. Emsley, *J. Am. Chem. Soc.* 2017, **139**, 10055.
- 90 J. Gong, M. Yang, X. Ma, R. D. Schaller, G. Liu, L. Kong, Y. Yang, M. C. Beard, M. Lesslie, Y. Dai, B. Huang, K. Zhu, T. Xu, *J. Phys. Chem. Lett.* 2016, **7**, 2879.
- 91 J. P. Perdew, A. Zunger, *Phys. Rev. B* 1981, **23**, 5048.
- 92 Y. Zhang, W. Yang, *J. Chem. Phys.* 1998, **109**, 2604.
- 93 J. P. Perdew, R. G. Parr, M. Levy, J. L. Balduz, *Phys. Rev. Lett.* 1982, **49**, 1691.
- 94 G. Miceli, W. Chen, I. Reshetnyak, A. Pasquarello, *Phys. Rev. B* 2018, **97**, 121112.
- 95 N. L. Nguyen, N. Colonna, A. Ferretti, N. Marzari, *Phys. Rev. X* 2018, **8**, 021051.
- 96 F. Ambrosio, J. Wiktor, F. De Angelis, A. Pasquarello, *Energy Environ. Sci.* 2018, **11**, 101.
- 97 K. Zheng, M. Abdellah, Q. Zhu, Q. Kong, G. Jennings, C. A. Kurtz, M. E. Messing, Y. Niu, D. J. Gosztola, M. J. Al-Marri, X. Zhang, T. Pullerits, S. E. Canton, *J. Phys. Chem. Lett.* 2016, **7**, 4535.
- 98 F. Ambrosio, D. Meggiolaro, E. Mosconi, F. De Angelis, *ACS Energy Lett.* 2019, **4**, 2013.
- 99 A. Filippetti, P. Delugas, A. Mattoni, *J. Phys. Chem. C* 2014, **118**, 24843.
- 100 T. M. Brenner, D. A. Egger, L. Kronik, G. Hodes, D. Cahen, *Nat. Rev. Mater.* 2016, **1**, 15007.

- 101 D. W. deQuilettes, S. M. Vorpahl, S. D. Stranks, H. Nagaoka, G. E. Eperon, M. E. Ziffer, H. J. Snaith, D. S. Ginger, *Science* 2015, **348**, 683.
- 102 C. W. Myung, J. Yun, G. Lee, K. S. Kim, *Adv. Energy Mater.* 2018, **8**, 1702898.
- 103 C. Quarti, G. Grancini, E. Mosconi, P. Bruno, J. M. Ball, M. M. Lee, H. J. Snaith, A. Petrozza, F. D. Angelis, *J. Phys. Chem. Lett.* 2014, **5**, 279.
- 104 A. M. A. Leguy, A. R. Goñi, J. M. Frost, J. Skelton, F. Brivio, X. Rodríguez-Martínez, O. J. Weber, A. Pallipurath, M. I. Alonso, M. Campoy-Quiles, M. T. Weller, J. Nelson, A. Walsh, P. R. F. Barnes, *Phys. Chem. Chem. Phys.* 2016, **18**, 27051.
- 105 F. Brivio, J. M. Frost, J. M. Skelton, A. J. Jackson, O. J. Weber, M. T. Weller, A. R. Goñi, A. M. A. Leguy, P. R. F. Barnes, A. Walsh, *Phys. Rev. B* 2015, **92**, 144308.
- 106 D. D. Sell, H. C. Casey, *J. Appl. Phys.* 1974, **45**, 800.
- 107 L. M. Herz, *ACS Energy Lett.* 2017, **2**, 1539.
- 108 Y. Kang, S. Han, *Phys. Rev. Appl.* 2018, **10**, 044013.
- 109 C. Quarti, E. Mosconi, F. De Angelis, *Phys. Chem. Chem. Phys.* 2015, **17**, 9394.
- 110 J. Even, L. Pedesseau, C. Katan, *J. Phys. Chem. C* 2014, **118**, 11566.
- 111 A. Mahata, D. Meggiolaro, F. De Angelis, *J. Phys. Chem. Lett.* 2019, **10**, 1790.
- 112 Z. Wang, Q. Lin, F. P. Chmiel, N. Sakai, L. M. Herz, H. J. Snaith, *Nat. Energy* 2017, **2**, 17135.
- 113 N. K. Noel, S. D. Stranks, A. Abate, C. Wehrenfennig, S. Guarnera, A.-A. Haghighirad, A. Sadhanala, G. E. Eperon, S. K. Pathak, M. B. Johnston, A. Petrozza, L. M. Herz, H. J. Snaith, *Energy Environ. Sci.* 2014, **7**, 3061.
- 114 E. Mosconi, P. Umari, F. De Angelis, *J. Mater. Chem. A* 2015, **3**, 9208.
- 115 F. Hao, C. C. Stoumpos, R. P. H. Chang, M. G. Kanatzidis, *J. Am. Chem. Soc.* 2014, **136**, 8094.
- 116 A. Pisanu, A. Mahata, E. Mosconi, M. Patrini, P. Quadrelli, C. Milanese, F. De Angelis, L. Malavasi, *ACS Energy Lett.* 2018, **3**, 1353.
- 117 G. E. Eperon, T. Leijtens, K. A. Bush, R. Prasanna, T. Green, J. T.-W. Wang, D. P. McMeekin, G. Volonakis, R. L. Milot, R. May, A. Palmstrom, D. J. Slotcavage, R. A. Belisle, J. B. Patel, E. S. Parrott, R. J. Sutton, W. Ma, F. Moghadam, B. Conings, A. Babayigit, H.-G. Boyen, S. Bent, F. Giustino, L. M. Herz, M. B. Johnston, M. D. McGehee, H. J. Snaith, *Science* 2016, **354**, 861.
- 118 A. Goyal, S. McKechnie, D. Pashov, W. Tumas, M. v. Schilfgaarde, V. Stevanović, *Chem. Mater.* 2018, **30**, 3920.
- 119 J. Im, C. C. Stoumpos, H. Jin, A. J. Freeman, M. G. Kanatzidis, *J. Phys. Chem. Lett.* 2015, **6**, 3503.
- 120 K. Galkowski, A. Surrente, M. Baranowski, B. Zhao, Z. Yang, A. Sadhanala, S. Mackowski, S. D. Stranks, P. Plochocka, *ACS Energy Lett.* 2019, **4**, 615.

- 121 M.-G. Ju, M. Chen, Y. Zhou, J. Dai, L. Ma, N. P. Padture, X. C. Zeng, *Joule* 2018, **2**, 1231.
- 122 A. Babayigit, D. Duy Thanh, A. Ethirajan, J. Manca, M. Muller, H.-G. Boyen, B. Conings, *Sci. Rep.* 2016, **6**, 18721.
- 123 A. Babayigit, A. Ethirajan, M. Muller, B. Conings, *Nat. Mater.* 2016, **15**, 247.
- 124 D. Ju, Y. Dang, Z. Zhu, H. Liu, C.-C. Chueh, X. Li, L. Wang, X. Hu, A. K. Y. Jen, X. Tao, *Chem. Mater.* 2018, **30**, 1556.
- 125 D. Zhao, Y. Yu, C. Wang, W. Liao, N. Shrestha, C. R. Grice, A. J. Cimaroli, L. Guan, R. J. Ellingson, K. Zhu, X. Zhao, R.-G. Xiong, Y. Yan, *Nat. Energy* 2017, **2**, 17018.
- 126 H. Cho, S.-H. Jeong, M.-H. Park, Y.-H. Kim, C. Wolf, C.-L. Lee, J. H. Heo, A. Sadhanala, N. Myoung, S. Yoo, S. H. Im, R. H. Friend, T.-W. Lee, *Science* 2015, **350**, 1222.
- 127 Y. Ling, Z. Yuan, Y. Tian, X. Wang, J. C. Wang, Y. Xin, K. Hanson, B. Ma, H. Gao, *Adv. Mater.* 2016, **28**, 305.
- 128 N. Yantara, S. Bhaumik, F. Yan, D. Sabba, H. A. Dewi, N. Mathews, P. P. Boix, H. V. Demir, S. Mhaisalkar, *J. Phys. Chem. Lett.* 2015, **6**, 4360.
- 129 M. R. Leyden, L. Meng, Y. Jiang, L. K. Ono, L. Qiu, E. J. Juarez-Perez, C. Qin, C. Adachi, Y. Qi, *J. Phys. Chem. Lett.* 2017, **8**, 3193.
- 130 J. VandeVondele, M. Krack, F. Mohamed, M. Parrinello, T. Chassaing, J. Hutter, *Comput. Phys. Commun.* 2005, **167**, 103.
- 131 J. P. Perdew, M. Ernzerhof, K. Burke, *J. Chem. Phys.* 1996, **105**, 9982.
- 132 C. Adamo, V. Barone, *J. Chem. Phys.* 1999, **110**, 6158.
- 133 A. Poglitsch, D. Weber, *J. Chem. Phys.* 1987, **87**, 6373.
- 134 O. A. Vydrov, T. Van Voorhis, *J. Chem. Phys.* 2010, **133**, 244103.
- 135 R. Sabatini, T. Gorni, S. de Gironcoli, *Phys. Rev. B* 2013, **87**, 041108.
- 136 S. Goedecker, M. Teter, J. Hutter, *Phys. Rev. B* 1996, **54**, 1703.
- 137 J. VandeVondele, J. Hutter, *J. Chem. Phys.* 2007, **127**, 114105.